ACS APPLIED MATERIALS & INTERFACES

Research Article

www.acsami.org

Three-Dimensional $NiCo_2O_4$@Polypyrrole Coaxial Nanowire Arrays on Carbon Textiles for High-Performance Flexible Asymmetric Solid-State Supercapacitor

Dezhi Kong,[†,‡] Weina Ren,[†] Chuanwei Cheng,[*,†] Ye Wang,[‡] Zhixiang Huang,[‡] and Hui Ying Yang[*,‡]

[†]Shanghai Key Laboratory of Special Artificial Microstructure Materials and Technology, School of Physics Science and Engineering, Tongji University, Shanghai 200092, P.R. China

[‡]Pillar of Engineering Product Development, Singapore University of Technology and Design, 8 Somapah Road, Singapore

Supporting Information

ABSTRACT: In this article, we report a novel electrode of $NiCo_2O_4$ nanowire arrays (NWAs) on carbon textiles with a polypyrrole (PPy) nanosphere shell layer to enhance the pseudocapacitive performance. The merits of highly conductive PPy and short ion transport channels in ordered $NiCo_2O_4$ mesoporous nanowire arrays together with the synergistic effect between $NiCo_2O_4$ and PPy result in a high specific capacitance of 2244 F g^{-1}, excellent rate capability, and cycling stability in $NiCo_2O_4$/PPy electrode. Moreover, a lightweight and flexible asymmetric supercapacitor (ASC) device is successfully assembled using the hybrid $NiCo_2O_4$@PPy NWAs and activated carbon (AC) as electrodes, achieving high energy density (58.8 W h kg^{-1} at 365 W kg^{-1}), outstanding power density (10.2 kW kg^{-1} at 28.4 W h kg^{-1}) and excellent cycling stability (~89.2% retention after 5000 cycles), as well as high flexibility. The three-dimensional coaxial architecture design opens up new opportunities to fabricate a high-performance flexible supercapacitor for future portable and wearable electronic devices.

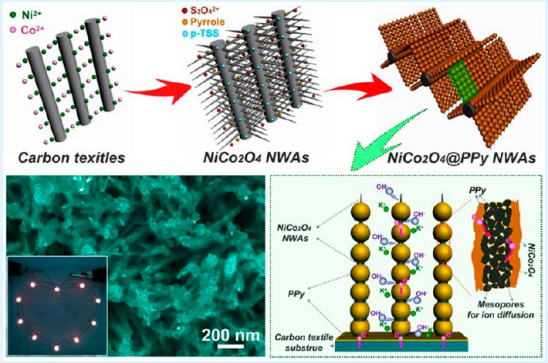

KEYWORDS: *$NiCo_2O_4$@PPy, coaxial, nanowire arrays, carbon textile, asymmetric supercapacitor*

INTRODUCTION

With the fast growth of wearable electronics devices, the investigation of a high-perfomance lightweight and flexible energy storage device has stimulated great research interest.[1−4] Supercapacitors (SCs) are attractive for energy storage devices due to their desirable advantages like outstanding power density (>10^4 W kg^{-1}), long lifespan (>10^5 times), good pulse charge/discharge rate (within seconds), and safety.[5−10] However, the application of SCs usually suffers from the low energy density. Referring to the equation $E = 1/2C(\Delta V)^2$, the energy density can be greatly improved by enhancing the device capacitance (C) and/or the cell potential windows (ΔV).[11,12] The capacitance is mainly related to the electrode materials, which can be boosted by selecting a proper electrode with tailored structures, while to increase the cell potential widow, an asymmetric supercapacitor (ASC) design with a pseudocapacitive (PC) electrode and an electric double-layer capacitive (EDLC) electrode is usually employed.[9,13]

Among the pseudocapacitive materials, ternary nickel cobaltite ($NiCo_2O_4$) has received considerable research attention due to that it has high theoretical capacity and low fabrication cost.[14,15] In the past few years, great effort has been devoted to boosting the capacitance of $NiCo_2O_4$ by exploring various nanostructures to provide large surface area plus short ion diffusion path.[16,17] However, the improvement is still limited by its poor electron transfer due to the conductivity problem. A conducting polymer, like polypyrrole (PPy), with high charge density and high electrical conductivity in doped states (10−100 S cm^{-1}) has also been widely explored as electrode for SCs.[18−21] Recent reports have demonstrated that the integration of metal oxide with PPy could greatly enhance the performance by improving the electron transport and ion diffusion issues.[22,23]

Herein, we report a facile route to fabricate 3D hierarchical $NiCo_2O_4$@PPy coaxial nanowire arrays on carbon textiles as electrode for high-performance SCs for the first time, where the mesoporous $NiCo_2O_4$ nanowires act as the highly capacitive "core" and uniform PPy nanospheres work as the well conductive "shell". This hybrid electrode provides several key advantages. First, the carbon textiles with excellent flexibility and conductivity are advantageous as a lightweight and flexible current collector. Second, the $NiCo_2O_4$ nanowire arrays on flexible conductive substrates with engineered mesopores are benefiting for ions access and transport. Third, the polypyrrole (PPy) nanospheres are uniformly coated onto each nanowire, which can significantly improve the electron transport within

Received: July 1, 2015
Accepted: September 15, 2015
Published: September 15, 2015

DOI: 10.1021/acsami.5b05908
ACS Appl. Mater. Interfaces 2015, 7, 21334−21346

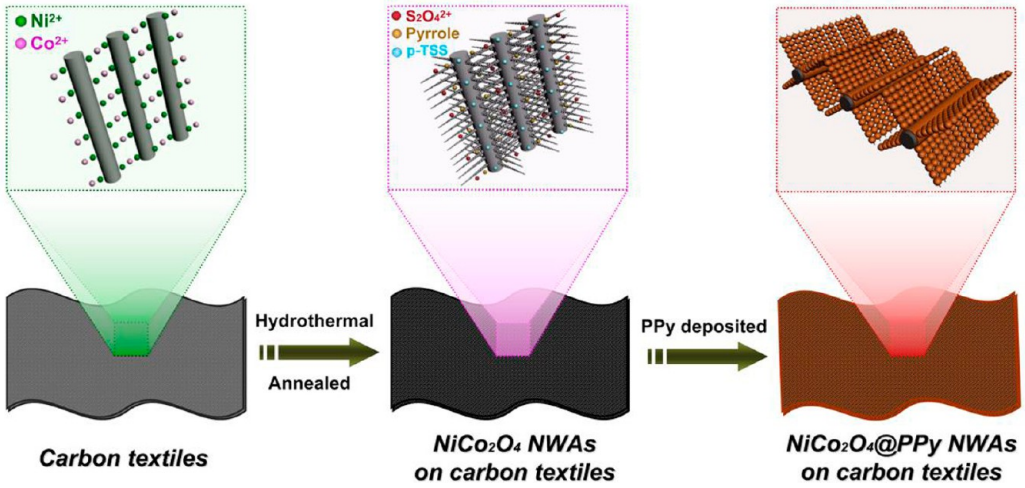

Figure 1. Schematic illustration of the fabrication process of hierarchical mesoporous $NiCo_2O_4$@PPy hybrid NWAs on carbon textiles.

every nanowire. Fourth, the mesoporous core−shell structure design allows electrolytes to penetrate every nanowire, and both the $NiCo_2O_4$ and PPy are involved in the redox reaction and contribute to the energy storage.[24] As such, the 3D PPy nanospheres incorporated 3D $NiCo_2O_4$ nanowire arrays ($NiCo_2O_4$@PPy NWAs) electrode delivers a specific capacitance of ∼2244 F g^{-1} at the current density of 1 A g^{-1} in solution electrolyte and good cycling stability. An asymmetric supercapacitor (ASC) is assembled by using the hybrid $NiCo_2O_4$@PPy NWAs and activated carbon (AC) as electrodes, which exhibits a high working voltage of 1.6 V, outstanding power density (10.2 kW kg^{-1} at 28.4 Wh kg^{-1}), and high energy density (58.8 W h kg^{-1} at 365 W kg^{-1}).

EXPERIMENTAL SECTION

Preparation of $NiCo_2O_4$ Nanowire Arrays. Self-supported $NiCo_2O_4$ NWAs on carbon textiles were fabricated using a modfied hydrothermal growth method.[17] Before use, carbon textiles were O_2 plasma treated for 60 s. Briefly, 1.16 g of $Co(NO_3)_2{\cdot}6H_2O$, 0.58 g of $Ni(NO_3)_2{\cdot}6H_2O$, and 1.44 g of urea were added into a mixed solution of ethanol/deionized water (with equal volume). The obtained homogeneous solution was transferred to 100 mL Teflon-lined stainless-steel autoclave lines, and then the pretreated carbon textiles (CeTech Co., Taiwan, 2.0 × 5.0 cm^2) were immersed in the mixed solution. The autoclave was sealed and kept at 100 °C for 8 h and then was cooled down to indoor temperature. Subsequently, the carbon textiles covered with NiCo-precursor NWAs were rinsed with deionized water several times and then dried in air at 60 °C. Finally, these samples were treated at 300 °C in air for 2 h to get well-defined crystallized $NiCo_2O_4$ NWAs.

Synthesis of 3D Coaxial $NiCo_2O_4$@PPy Nanowire Arrays. Typically, 1.5 mmol (∼0.285 g) of sodium *p*-toluenesulfonate (p-TSS, $C_7H_7SO_3Na$) was first mixed with 20 mL of DI water/ethanol (1:1, v/v). Then 0.116 g of pyrrole monomer was added with stirring, until a homogeneous mixture solution is formed (denoting as solution A). Meanwhile, 3.75 mmol (∼0.93 g) of ammonium persulfate $(NH_4)_2S_2O_8$) was dissolved in 30 mL of deionized water under vigorous stirring to obtain a homogeneous mixture solution B. Subsequently, the carbon textiles (2.0 × 5.0 cm^2) with $NiCo_2O_4$ NWAs grown on them were tilt-placed in a clean beaker, and then solution A was slowly dropped onto the carbon textiles with a spring to ensure that the carbon textiles was completely infiltrated. After 5 min, solution B was also dropped in the same manner, and the polymerization was carried out at 0−5 °C. The sample was subsequently left in the dark for 0.5−3.0 h before rinsing with deionized water and methanol successively to remove residues. Finally, the obtained product was dried in a vacuum oven at 80 °C overnight.

Characterizations. The morphology, size, and chemical composition of the samples were observed using field-emission scanning electron microscope (FESEM, JSM-7600F, JEOL Inc., Japan) equipped with an energy dispersive X-ray spectrometry (EDX), and the structures of the samples were executed by transmission electron microscopy (TEM, JEM-2010, JEOL Inc., Japan). The phase of the as-synthesized products was characterized by XRD with Cu Kα radiation (λ = 1.5418 Å, 40 kV, and 30 mA). The nitrogen adsorption−desorption isotherms were obtained at 77 K on a Micromeritics NOVA 4200e system. The surface area was obtained using the Brunauer−Emmett−Teller (BET) method, and the pore size distribution curve was obtained by Barrett−Joyner−Halenda (BJH) method from the adsorption branch isotherms. Raman spectra were conducted with a WITEC CRM200 Raman system, and the excitation source is a 532 nm laser using a 100× objective lens. The chemical compositions and the valence states of $NiCo_2O_4$@PPy are investigated by an X-ray photoelectron spectroscopy (XPS) spectrum using a PerkinElmer model PHI 5600 XPS system..

Electrochemical Performance Measurements. The electrochemical performances of as-prepared samples were evaluated using cyclic voltammetry (CV), galvanostatic charge−discharge, and electrochemical impedance spectroscopy (EIS) measurements on an electrochemical workstation (CHI 760D, Chenhua) by the three-electrode cell in 3 M KOH aqueous electrolytes. The $NiCo_2O_4$@PPy hybrid and $NiCo_2O_4$ NWAs on carbon textiles were directly used as the working electrode, in which Pt foil and Ag/AgCl were served as counter electrode and reference electrode, respectively. The EIS measurements were conducted with a frequency range from 10^5 Hz to 10^{-2} Hz and a voltage amplitude of 5 mV at open-circuit potential. The specific capacitance (C, F g^{-1}), energy density (E, W h kg^{-1}), and power density (P, W kg^{-1}) were calculated according to the following equations:[25,26]

$$C = \frac{I\Delta t}{m\Delta V} \tag{1}$$

$$E = \frac{1}{7.2}C(\Delta V)^2 \tag{2}$$

$$P = 3600\frac{E}{\Delta t} \tag{3}$$

The solid-state asymmetric supercapacitor devices (ASCs) were assembled using $NiCo_2O_4$@PPy NWAs as positive electrode and an activated carbon (AC) as negative electrode. PVA/KOH gel was obtained by mixing PVA (6 g) and KOH (3 g) in 80 mL deionized water and heated at 95 °C under vigorous stirring for 2 h. $NiCo_2O_4$@

DOI: 10.1021/acsami.5b05908
ACS Appl. Mater. Interfaces 2015, 7, 21334−21346

PPy NWAs and AC electrodes were immersed in the gel about 5 min and then assembled together. The CV and galvanostatic charge−discharge measures were conducted in the potential range of 0 to 1.6 V at scan rates of 2−100 mV s^{-1} and at current densities of 2−20 mA cm^{-2}, respectively. The effective area of the ASCs immersed into the solid-state electrolyte is controlled to be about 2.0 × 4.0 cm^2. The volumetric capacitance (C_{vc}, F cm^{-3}) and specific capacitance (C_{sc}, F g^{-1}) of the ASC devices were determined based on the following equations:[27,28]

$$C_{VC} = 4\frac{I}{A}\frac{dt}{dV} \quad \text{or} \quad C_{SC} = 4\frac{I}{m}\frac{dt}{dV} \tag{4}$$

where I means the discharge current (mA), A is he geometrical volumetric of the electrode (cm^3), m represents the total mass of the two electrode active materials (g), and dV/dt is the slope of the discharge curve (V s^{-1}).

RESULTS AND DISCUSSION

The typical preparation process of the 3D $NiCo_2O_4$@PPy coaxial NWAs electrode is schematically illustrated in Figure 1. First, mesoporous $NiCo_2O_4$ NWAs were grown vertically on carbon textiles using a modified hydrothermal and postannealing route. In a subsequent step, the PPy nanospheres layer (Figure S2a) was wrapped onto the mesoporous $NiCo_2O_4$ nanowire arrays using a chemical polymerization process. The corresponding real color pictures of the samples are shown in Figure S1a. The images in Figure S1b−d demonstrate the excellent flexibility of the $NiCo_2O_4$@PPy electrode.

Figure 2 presents the SEM images of the $NiCo_2O_4$ and $NiCo_2O_4$@PPy NWAs grown on the carbon textiles. Obviously, the top-view (Figure 2a,b) and cross-sectional SEM (Figure 2c) images indicate that well-aligned $NiCo_2O_4$ NWAs are grown on the carbon textiles. A careful examination reveals that the wire-like $NiCo_2O_4$ nanostructure are with diameters of ∼40 nm in the middle part and length of ∼2 μm, and each nanowire is assembled of any nanoparticles, forming a highly mesoporous structure. After the PPy growth, one layer of the PPy nanospheres is regularly distributed onto each nanowire, which looks like a bunch of ice-sugar gourds, as displayed in Figure 2d−f. From the enlarged view (inset of Figure 2d), we can observe that the PPy nanospheres are interconnected with each other but still could not fully cover the whole mesoporous $NiCo_2O_4$ nanowires, and some tip parts of the $NiCo_2O_4$ NWAs are exposed (see the circle labeled), which was further confirmed with the TEM image (Figure 3c). The pores or voids between the nanowires and nanospheres are facilitating for the electrolyte access during the process of charging and discharging. Moreover, the pure PPy nanospheres on carbon textiles were also provided for comparison (see Figure S2b,2c).

Further information about the $NiCo_2O_4$ and $NiCo_2O_4$@PPy NWAs were recorded by the TEM and HR-TEM. From the TEM image of $NiCo_2O_4$ NWAs, in Figure 3a, it can be clearly seen that the diameter of the nanowires varies from 60 nm on the bottom to 10 nm at the tip. The enlarged view inset of Figure 3a indicates that the nanowires are assembled by a number of nanoparticles with many mesopores. The HR-TEM image in Figure 3b presents two sets of lattice fringes with interplanar spacings of 0.23 and 0.25 nm, respectively, corresponding to the (222) and (311) planes of $NiCo_2O_4$. The SAED pattern inset in Figure 3b suggests that the $NiCo_2O_4$ nanowires are polycrystalline, which is corresponding to the spinel $NiCo_2O_4$ crystal structure.[29] The TEM image of the $NiCo_2O_4$@PPy nanowires in Figure 3c clearly demonstrates

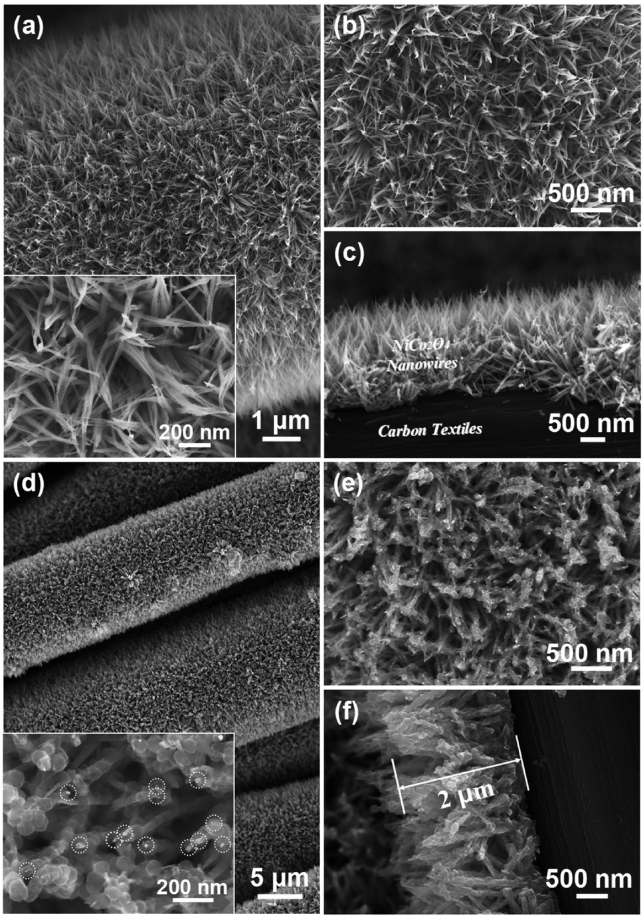

Figure 2. SEM images of $NiCo_2O_4$ NWAs: (a and b) top view and (c) cross-section view; $NiCo_2O_4$@PPy NWAs: (d and e) top view and (f) cross-section view; the insets of (a) and (d) are the high-magnification SEM images.

that the PPy spheres are uniformly deposited on the surface of each nanowire, with the layer thickness varying from few nanometers to ∼20 nm. Meanwhile, the HR-TEM image in Figure 3d indicates that the PPy is amorphous.

The crystal structures of as prepared pure PPy, $NiCo_2O_4$ NWAs, and $NiCo_2O_4$@PPy NWAs on the carbon textiles were recorded by XRD and Raman characterizations. As displayed in Figure 4a, the pure PPy exhibits two broad peaks at $2\theta \approx 26°$ (i.e., d = 0.34 nm) and 42.5°, which indicates that it is amorphous phase.[30] The diffraction peaks at 18.75, 31.27, 36.26, 44.19, 59.35, 65.23, and 76.70° collected from $NiCo_2O_4$ NWAs and $NiCo_2O_4$@PPy NWAs can be well indexed with spinel phase of $NiCo_2O_4$ (JCPDS Card No. 20-0718).[31,32] Moreover, the two peaks marked by "#" belong to the carbon textiles. To further confirm the structural features of the products, Raman spectroscopy was carried out and is shown in Figure 4b. The $NiCo_2O_4$ NWAs exhibit four apparent peaks at around 186 cm^{-1}, 480 cm^{-1}, 529 cm^{-1}, and 668 cm^{-1}, which are assigned to the F_{2g}, E_g, F_{2g}, and A_{1g} models of $NiCo_2O_4$, respectively.[33,34] Beyond these bands, the other peaks belong to the PPy. The high intensity peak at 1600 cm^{-1} is attributed to symmetric stretching of the aromatic C═C ring, the double peaks at ∼1380 and 1320 cm^{-1} are related to the ring-stretching mode of PPy, the peak at ∼1050 cm^{-1} is attributed to C—H in-plane deformation, and the peaks at ∼940 and ∼990 cm^{-1} are corresponding to the ring deformation

DOI: 10.1021/acsami.5b05908
ACS Appl. Mater. Interfaces 2015, 7, 21334−21346

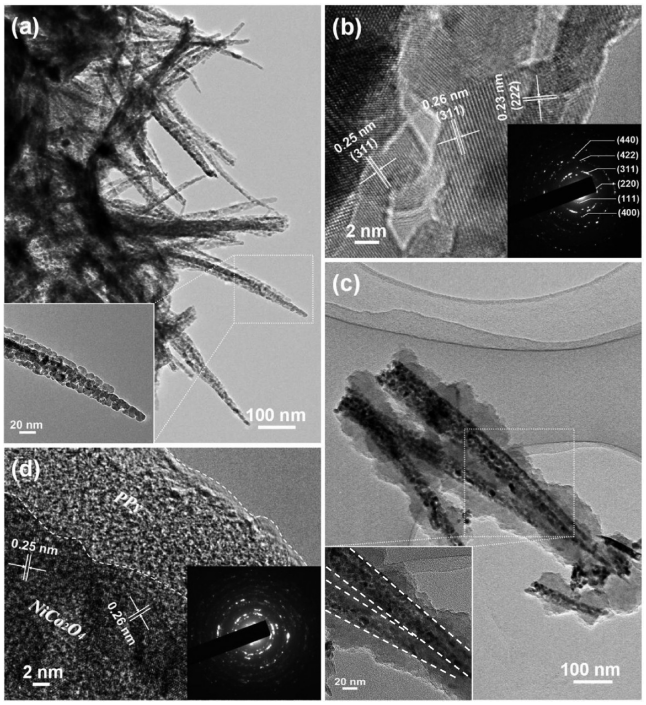

Figure 3. TEM image (a) and HR-TEM image (b) of $NiCo_2O_4$ NWAs; TEM image (c) and HR-TEM image (d) of $NiCo_2O_4$@PPy NWAs; the insets of (a) and (c) are the corresponding SAED patterns from $NiCo_2O_4$ and $NiCo_2O_4$@PPy NWAs.

associated with dications (bipolaron) and radical cations (polarons), respectively.[35,36]

The EDX mapping results in Figure 5a clearly suggest that the elements Ni, Co, O, C, and N are homogeneously distributed, confirming the $NiCo_2O_4$ core/PPy shell hierarchical structure. The EDS spectrum result shown in Figure 5b is consistent with the SEM elemental mapping and further verifies the uniform presence of Co, Ni, O, C, N, and S (with a Co/Ni molar ratio of ~2.0). The trace of the S element might be introduced into the interlayer of PPy during the polymerization process. Furthermore, the BET surface area value of the $NiCo_2O_4$@PPy NWAs is estimated to be 97.48 $m^2\ g^{-1}$. As shown in Figure 5c, a distinct hysteresis loop can be observed in the range of 0.6−1.0 P/P_0, which suggests the presence of a mesoporous structure for the nanowires. As shown in inset of Figure 5c, the pore size distribution of the sample was calculated using desorption isotherm by Barret−Joyner−Halenda (BJH) method. The $NiCo_2O_4$@PPy NWAs show narrow and ordered distributions of pores at ~5.06 and 14.80 nm, and the sample pore volume of NWAs is ~0.32 $cm^3\ g^{-1}$.

The chemical compositions and the valence states of $NiCo_2O_4$@PPy hybrid composites were further investigated by X-ray photoelectron spectroscopy. The full scan spectrum of the $NiCo_2O_4$@PPy NWAs in Figure 5d demonstrates the presence of Co, Ni, O, C, N, and S elements, without any other impurities. The XPS spectrum of the Ni 2p core-level was shown in Figure S3a, which is best fitted with two spin−orbit doublets, characteristic of Ni^{2+} and Ni^{3+}, and two shakeup satellites (marked as "Sat."). The fitting peaks at 855.1 and 872.8 eV are indexed to Ni^{2+}, whereas other fitting peaks at 856.3 and 874.3 eV are assigned to Ni^{3+}.[9,37] Similarly, the core-level spectrum of Co 2p were curve fitted and are shown in Figure S3b. There are four multiplet peaks for Co 2p observed in the spectra, and peaks corresponding to 781.2 and 796.1 eV are ascribed to Co^{2+}, whereas 779.3 and 794.9 eV are assigned to Co^{3+}.[37,38] As shown in the inset of Figure 5d, the N 1s spectrum can be deconvoluted into three components. The binding energies of 398.3, 399.3, and 401 eV are assigned to —C═N—, —NH—, and —NH^+—, respectively.[9,39,40] The deconvolution peaks (inset of Figure 6d) of the O 1s spectrum are resolved into two components, which are centered on 529.1 and 530.8 eV. One peak centered at 529.1 eV is attributed to the O^{2-} forming oxides with Ni and Co, while the other one is corresponding to the OH^-. The XPS spectrum of C 1s core-level from $NiCo_2O_4$@PPy NWAs (Figure S3c) is also resolved into four peaks at 284.1, 285.1, 286.2, and 287.8 eV, which can be assigned to β-carbon, α-carbon, C═N bonds, and —C═N^+ bonds, respectively.[41] Figure S3d shows the XPS spectra of S 2p

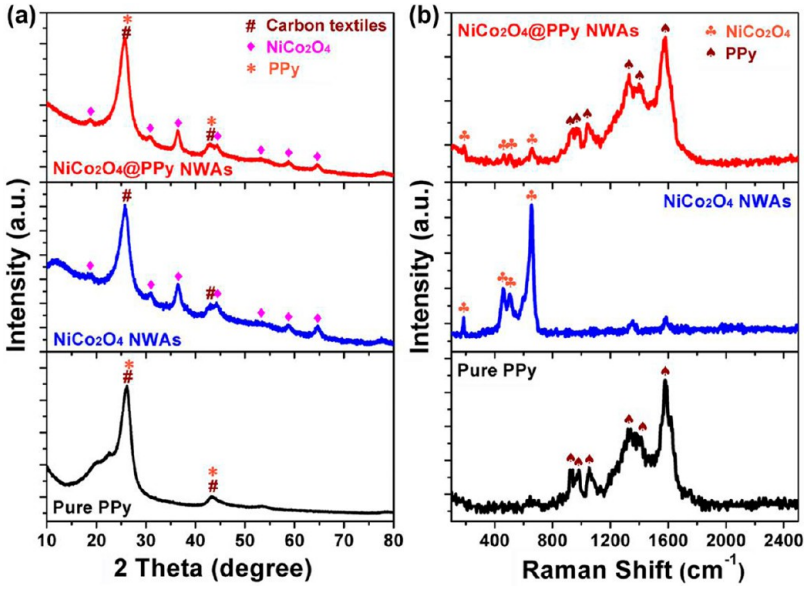

Figure 4. (a) XRD patterns and (b) Raman spectra of pure PPy, $NiCo_2O_4$ NWAs, and $NiCo_2O_4$@PPy NWAs.

DOI: 10.1021/acsami.5b05908
ACS Appl. Mater. Interfaces 2015, 7, 21334−21346

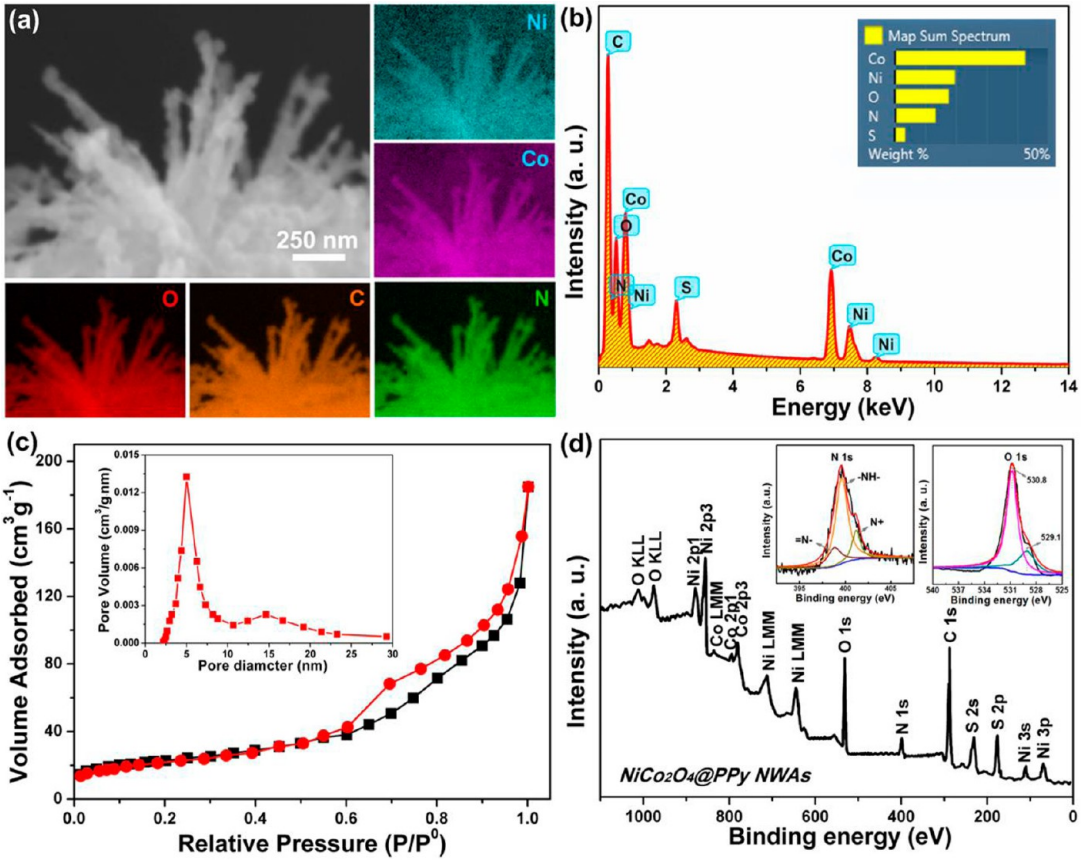

Figure 5. (a) SEM image and corresponding EDX elemental mappings of Ni, Co, O, C, and N for the $NiCo_2O_4$@PPy NWAs; (b) EDX microanalysis and the corresponding elemental contents on selected areas of the $NiCo_2O_4$@PPy NWAs; (c) nitrogen adsorption−desorption isotherm and BJH adsorption pore-size distribution for the obtained $NiCo_2O_4$@PPy NWAs without carbon textiles; (d) XPS survey spectra of $NiCo_2O_4$@PPy NWAs hybrid composites.

double peaks; the binding energies of S $2p_{3/2}$ and S $2p_{1/2}$ were observed at ∼163.8 eV and ∼164.9 eV, respectively.[9,42]

The evolution of $NiCo_2O_4$ NWAs with different reaction times was investigated by tracking the product morphology taken at different reaction stages. In the beginning, the carbon textiles show smooth surface after plasma treatment (Figure S4a). When the hydrothermal reaction was extended to 2 h, some nanoparticles and nanorods are uniformly formed on the surface of the carbon textiles (Figure S4b). With the reaction times increased to 5 h, the nanoparticles will grow anisotropically into sparse nanowires (Figure S4c). These nanowire arrays are formed, arising from the heterogeneous nucleation and growth via the hydrolysis of urea in aqueous solution, which decreases the interfacial nucleation energy on the substrate. Further increasing the hydrothermal reaction time to 8 h, these nanowires became dense and connected with each other (Figure S4d).

To optimize the thickness of PPy shell layers, the effects of growth times on the morphology and thickness of PPy are discussed. As shown in Figure 6, at initial deposition stage (0.5 h, Figure 6b), the PPy nanoparticles begin to attach to the top on the nanowire arrays. As the deposition time increase (1.5 h, Figure 6c), the PPy nanospheres start to grow large accordingly but still not completely cover the whole mesoporous $NiCo_2O_4$ NWAs. With the deposition time increased up to 3 h (Figure 6d), a tight coating of PPy nanospheres with high density was produced on the whole surface of $NiCo_2O_4$ NWAs, without an open porous structure. The corresponding growth mechanism can be illustrated in Figure 6e. In the early stage, only few pyrrole monomers are polymerized and nucleated, and rare PPy nanoparticles are found on the surface of $NiCo_2O_4$ NWAs. With the time increased to 1.5 h, the PPy nanospheres layer become dense and thick due to more pyrrole monomers being involved in the polymerization process and deposited on the surface. With further increasing the times to 3 h, the PPy nanospheres layer covered the whole surface of $NiCo_2O_4$ NWAs. To verify the universality of the chemical bath deposition method in synthesizing the PPy shell, we extended the method to $NiCo_2O_4$ nanoflake arrays as the support "core" materials (Figure S5). With increasing the chemical bath deposition times of PPy, the PPy nanospheres grown on surfaces of the $NiCo_2O_4$ NFAs became thicker and tighter.

The electrochemical storage applications of as-prepared products are first carried out by testing them as electrodes for supercapacitors in a three-electrode electrochemical system. Figure 7a presents a group of cyclic voltammetry (CV) curves for different hybrid $NiCo_2O_4$@PPy NWAs electrodes with different PPy polymerization times. It is observed that the current response increases with the PPy polymerization reaction times, resulting in enhancement of the capacitance. However, further increase in the polymerization reaction time up to 3.0 h leads to the decrease of the total capacitance (as shown inset of Figure 7a), which might be due to the thick and dense PPy layer could prevent the ion penetration to the inner core of $NiCo_2O_4$ NWAs. The charge−discharge curves of various hybrid $NiCo_2O_4$@PPy NWAs electrodes tested at

DOI: 10.1021/acsami.5b05908
ACS Appl. Mater. Interfaces 2015, 7, 21334−21346

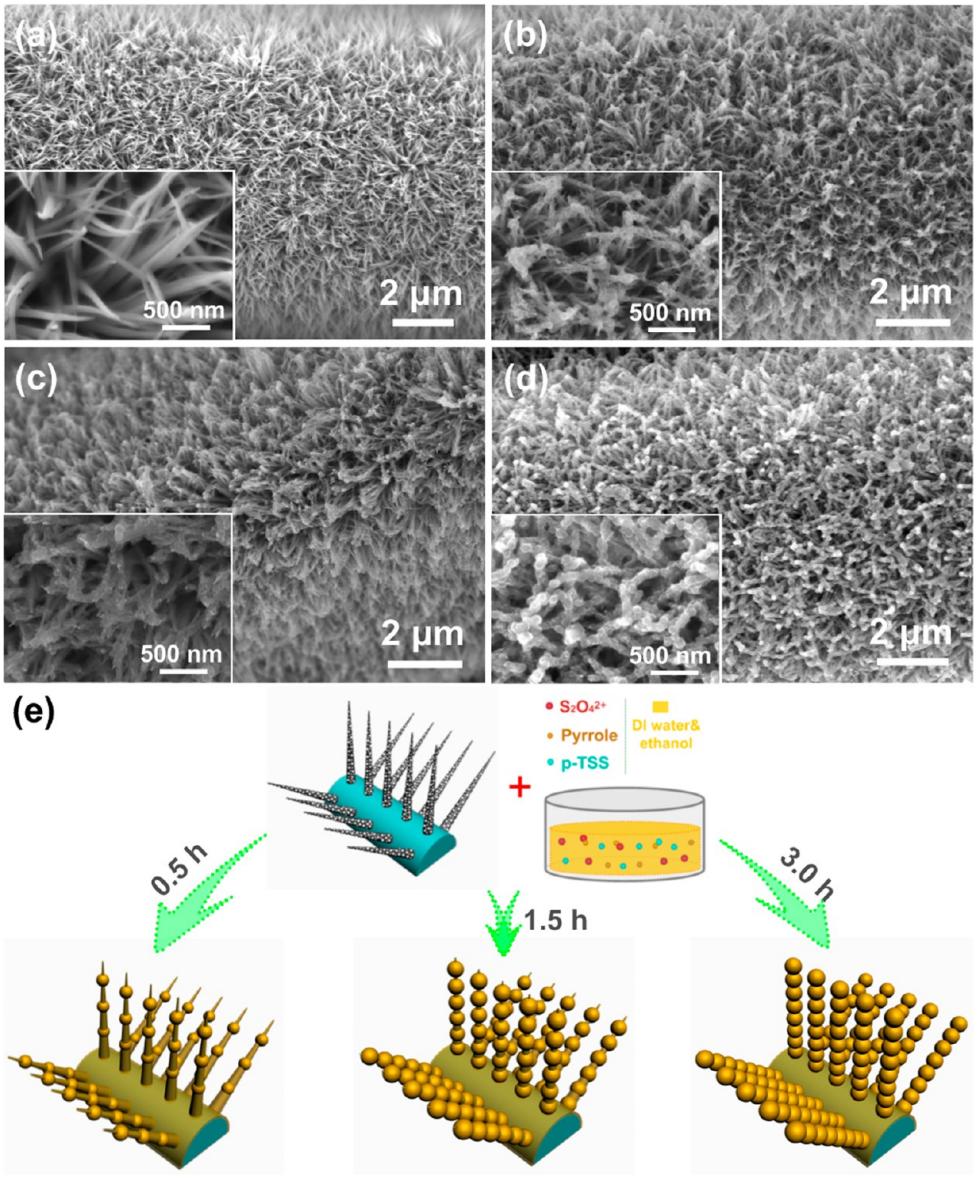

Figure 6. SEM images of the $NiCo_2O_4$@PPy NFAs synthesized at different reaction times: (a) 0 h, (b) 0.5 h, (c) 1.5 h, and (d) 3.0 h, respectively. (e) Proposed mechanism for the effect of deposited time on the morphology construction.

current densities of 2 A g^{-1} are also shown in Figure S6a, where the $NiCo_2O_4$@PPy NWAs obtained after 1.5 h polymerization exhibit the highest specific capacitance and lowest internal resistance (IR). In the following performance tests, we mainly focused on the $NiCo_2O_4$@PPy NWAs obtained with 1.5 h polymerization times.

To confirm the superiority of the hierarchical $NiCo_2O_4$@PPy NWAs, Figure 7b compares the CV curves of carbon textiles, pure PPy, $NiCo_2O_4$ NWAs, and $NiCo_2O_4$@PPy NWAs on carbon textiles collected at scan rates of 10 mV s^{-1}, respectively. A pair of redox peaks are observed for the pristine $NiCo_2O_4$ NWAs electrodes, which are mainly due to the faradaic reactions and can be expounded by the following equations:[9,43] $NiCo_2O_4 + OH^- + 2H_2O \leftrightarrow NiOOH + 2CoOOH + H_2O + e^-$, $CoOOH + OH^- \leftrightarrow CoO_2 + H_2O + e^-$. As expected, the $NiCo_2O_4$@PPy nanocomposite electrode exhibits significantly higher current densities and electrochemical capacitance in contrast to that of the unitary $NiCo_2O_4$ and PPy electrodes due to the synergistic effects between $NiCo_2O_4$ and PPy: first, the conductive polypyrrole (PPy) is able to improve the electrical conductivity of the entire electrode, as a result in improving electron transport rate; second, both the core $NiCo_2O_4$ and the PPy shell layer contribute to the pseudocapacitance. Noting that, the integrated CV area for the carbon textiles electrode is negligible compared with the other three electrodes (see inset of Figure 7b). The galvanostatic charge−discharge curves for pure PPy, $NiCo_2O_4$ NWAs, and $NiCo_2O_4$@PPy NWAs electrodes were further examined at a current density of 2 A g^{-1} (Figure S6b). As a consequence, the $NiCo_2O_4$@PPy NWAs electrode exhibits the longest discharging times, indicating its highest capacitances. Besides, the internal resistance (IR) of the $NiCo_2O_4$@PPy NWAs hybrid electrode was ~0.016 V, which is smaller than that of the $NiCo_2O_4$ NWAs electrode (0.03 V), further indicating that the PPy shell can availably decrease the total resistance, as a result in improving the charge transport and electron collection efficiency.

To study the influence of scan rates on the electrochemical performance, the CV curves of the $NiCo_2O_4$@PPy NWAs

DOI: 10.1021/acsami.5b05908
ACS Appl. Mater. Interfaces 2015, 7, 21334−21346

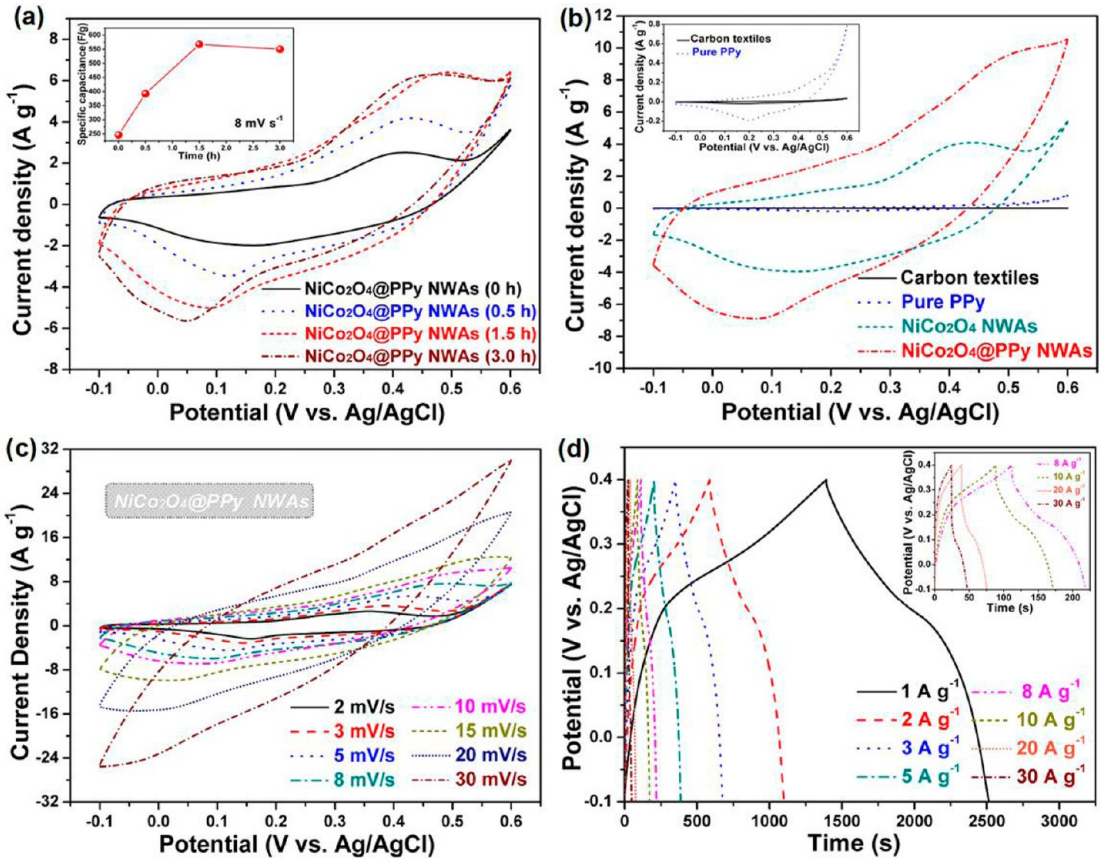

Figure 7. (a) Comparison of CV curves at a scan rates of 8 mV s^{-1} for $NiCo_2O_4$@PPy NWAs synthesized at different times in the reaction: 0 h, 0.5 h, 1.5 h, and 3 h, respectively; (b) comparison of CV curves for carbon textiles, pure PPy, $NiCo_2O_4$ NWAs, and $NiCo_2O_4$@PPy NWAs, recorded at a scan rate of 10 mV s^{-1}; (c) CV and (d) galvanostatic charge−discharge curves of the $NiCo_2O_4$@PPy NWAs at different scan rates and different current densities in 3 M KOH aqueous solution, respectively.

electrode with various scan rates ranging from 2 to 30 mV s^{-1} are shown in Figure 7c. A pair of redox peaks are clearly observed from all the CV curves, which is mainly originated from the reversible faradaic redox reactions correlated to M−O/M−O−OH (M = Ni or Co).[44] Interestingly, with the sweep rates increase, the current density increases and the positions of anodic and cathodic peaks shift to a more anodic and cathodic direction, respectively, indicating that the fast and reversible redox reactions occurring at the electro/electrolyte interface. The $NiCo_2O_4$@PPy NWAs were also carried out using galvanostatic charge−discharge tests within the voltage range of −0.1−0.4 V, as shown in Figure 7d. It can be seen that all the curves are nonlinear and asymmetrical at different current densities from 1 to 30 A g^{-1}, which confirms the pseudocapacitive behavior of the hybrid electrode. Moreover, these charge/discharge voltage plateaus match well with the redox peaks observed in the CV curves. As a comparison, the CV and galvanostatic charge−discharge curves of $NiCo_2O_4$ NWAs electrodes at various scan rates (from 2 to 30 mV s^{-1}) and current densities (from 1 to 30 A g^{-1}) are presented in Figure S7a,b, respectively. These results demonstrate that the 3D hierarchical nanostructure arrays with the PPy shell are beneficial to improve the capacitive performance of $NiCo_2O_4$ NWAs electrodes.

As displayed in Figure 8a, the specific capacitance of the $NiCo_2O_4$@PPy NWAs electrode was much higher than the $NiCo_2O_4$ NWAs electrode at different discharging current densities. The specific capacitance values obtained for the hybrid $NiCo_2O_4$@PPy NWAs electrode was 2244.5 F g^{-1} at 1 A g^{-1}, which is considerably higher than the single $NiCo_2O_4$ NWAs electrode (1189.4 F g^{-1}). When the current density is enhanced up to 30 A g^{-1}, the $NiCo_2O_4$@PPy NWAs electrode still has a specific capacitance of 1358 F g^{-1}, indicating its excellent rate capability (~60.5%). In contrast, the capacity retention of the pure $NiCo_2O_4$ NWAs electrode is only ~52.6% at 30 A g^{-1}.

The cycling performance is another important merit for the supercapacitors in practical use. Figure 8b depicts the cycling curves for the two types of electrodes at a rate of 3 A g^{-1}. The $NiCo_2O_4$@PPy NWAs electrode is able to maintain a capacity retention of 89.5% after 5000 cycles and 82.9% after 10000 cycles, respectively. In addition, during the long-time cycling, the Coulombic efficiency of the $NiCo_2O_4$@PPy NWAs hybrid electrode is mostly above 97%, indicating a high efficiency of the rapid electron transfer for charge storage and delivery (Figure S7c). However, the $NiCo_2O_4$ NWAs electrode shows higher capacitance decay of about 10.9% after 5000 cycles. The main reason for the capacitance decay in $NiCo_2O_4$ is the dissolution of $NiCo_2O_4$ into the electrolyte, whereas the conducting polymers lose their capacitance resulting from the structure defects caused by the repetitive swelling/shrinkage of the polymer chains.[45] The enhanced cycling stability of $NiCo_2O_4$@PPy NWAs can be attributed to the coaxial structure, in which the $NiCo_2O_4$ core offers a solid skeleton to interlink the PPy nanospheres, and in turn the PPy layer protects the $NiCo_2O_4$ from dissolving in electrolyte. Actually,

DOI: 10.1021/acsami.5b05908
ACS Appl. Mater. Interfaces 2015, 7, 21334−21346

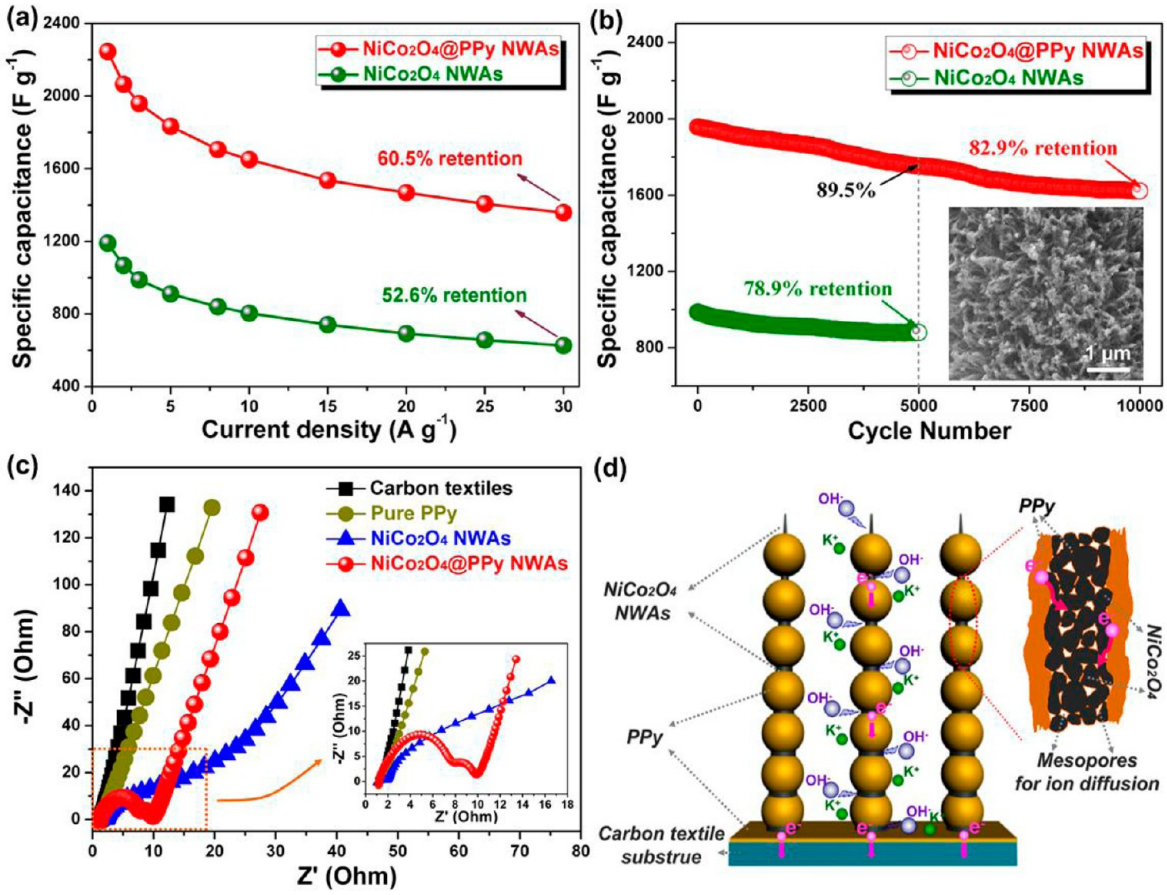

Figure 8. (a) Current−density dependence of the specific of the $NiCo_2O_4$ NWAs and $NiCo_2O_4$@PPy NWAs electrode; (b) cycling performance of the $NiCo_2O_4$@PPy NWAs electrodes (10000 cycles), compared to $NiCo_2O_4$ NWAs electrodes (5000 cycles); (c) Nyquist plots of the specific of the carbon textiles, pure PPy, $NiCo_2O_4$ NWAs, and $NiCo_2O_4$@PPy NWAs electrode at open circuit potential; the inset of (c) is the enlarged impedance spectrum of these electrodes at high frequencies; (d) schematic representation of rechargeable supercapacitor based on $NiCo_2O_4$@PPy NWAs on carbon textiles.

we checked the composite morphology of $NiCo_2O_4$@PPy NWAs after 10000 charge−discharge cycles and found that the pristine 3D structures were still well-maintained (inset of Figure 8b). As a result, the mutual cooperation ensures the structural integrity of $NiCo_2O_4$@PPy nanocomposites and thus the long-term cycling stability.

Electrochemical impedance spectroscopy (EIS) tests have been further conducted to observe the intrinsic mechanism on the dramatic performance improvement of the $NiCo_2O_4$@PPy nanocomposites. Figure 8b depicts the resulting Nyquist plots of the EIS spectra for the carbon textiles, pure PPy, $NiCo_2O_4$ NWAs, and $NiCo_2O_4$@PPy NWAs composite electrodes at open circuit potential. All the EIS spectra are consisted of one (or two) semicircles in the high-frequency region and a spike in the low-frequency region, which can be simulated by an equivalent circuit (Figure S7d). In the equivalent circuit, the ohmic resistance R_S is determined by both the electrolyte resistance and the electrode electronic resistance and deduced by high frequency cut on the real axis.[21,27] As for the above four electrodes, the R_S values are very close to be 1.2−1.3 Ω, which is reasonable because the electrochemical properties are measured in the same electrolyte solution. The charge transfer resistance R_{ct}, which is deduced by the diameter of the semicircle.[46] Evidently, the R_{ct} of the hybrid $NiCo_2O_4$@PPy NWAs electrode (~8.8 Ω) is lower than that of the pristine $NiCo_2O_4$ NWAs electrode (~13.7 Ω). Interestingly, the EIS of $NiCo_2O_4$@PPy NWAs electrode is composed of two semicircles, which can be attributed to the formation of the solid electrolyte interface (SEI) from both the $NiCo_2O_4$ core and PPy shell surfaces. The straight line in the low-frequency range represents the Warburg resistance (Z_W), which is described as a diffusive resistance of the OH^- ion within the electrode materials pores.[47] After 10000 cycles, the R_{ct} slightly increases from 8.8 to 11.2 Ω (Figure S7d), indicating that long-time charge−discharge processes have not damaged the $NiCo_2O_4$@PPy hybrid electrode.

The rational design and the charge storage processes of the coaxial $NiCo_2O_4$@PPy NWAs structure for effective electrochemical utilization are schematically illustrated in Figure 8d. A series of experimental results reveal that the performance improvement can be attributed to the following aspects: (i) Both the $NiCo_2O_4$ and PPy exhibit excellent pseudocapacitive behaviors in the same KOH alkaline electrolyte, thereby cocontributing to the overall capacitance significantly. (ii) The 1D nanowire arrays could provide short solid-state pathways for the ion diffusion and rapid charge collection/transfer; moreover, $NiCo_2O_4$ cores have an intimate electrical connection to the PPy nanospheres, which builds a reliable conductive network for fast electron transport throughout the electrode. Therefore, a maximum harvest of pseudocapacitance from $NiCo_2O_4$ and PPy components is promoted. (iii) The mesoporous nanostructure creates additional channels for

DOI: 10.1021/acsami.5b05908
ACS Appl. Mater. Interfaces 2015, 7, 21334−21346

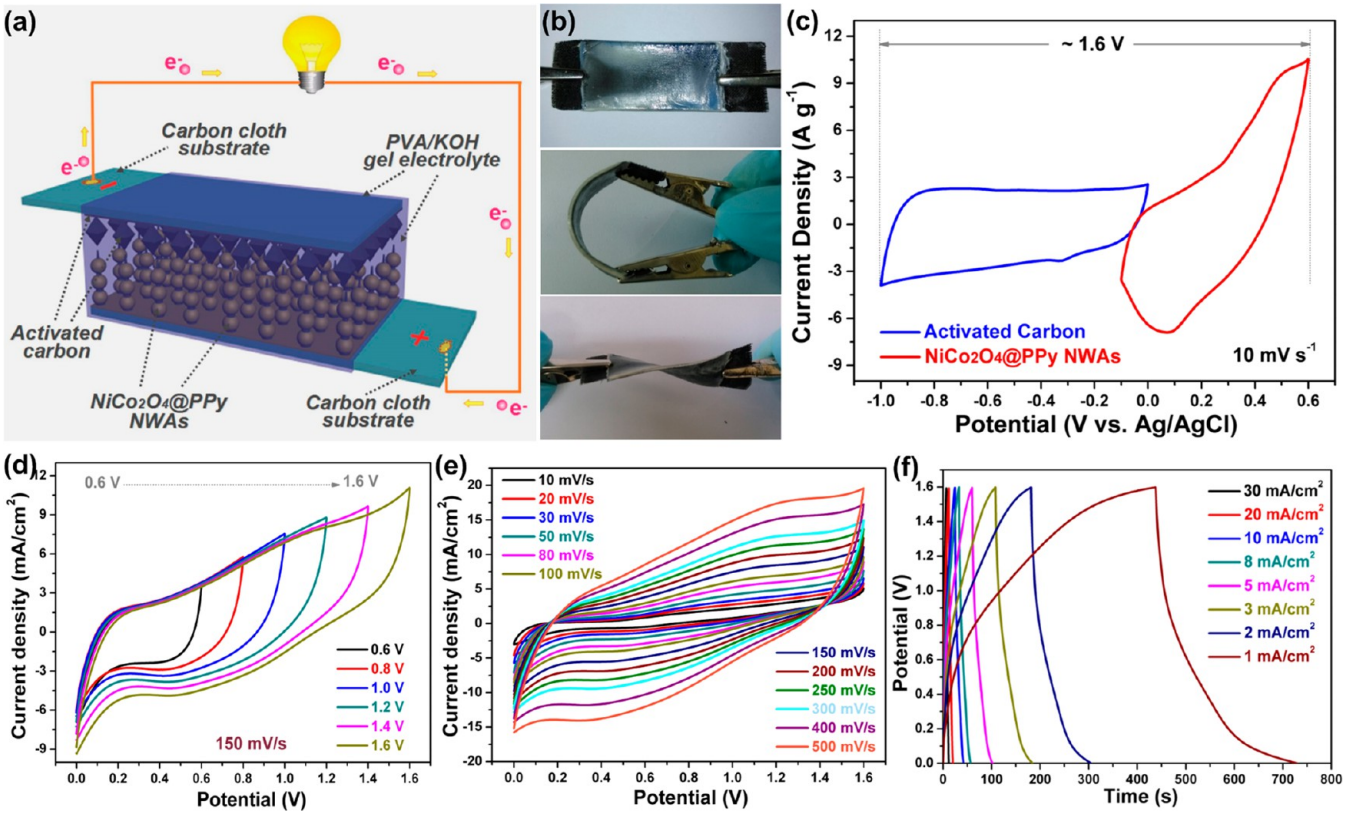

Figure 9. (a) Schematic illustration of an ASC that consists of the $NiCo_2O_4$@PPy NWAs positive electrode, electrolyte-soaked separator, and AC negative electrode. (b) Digital photos: the device was straightened, bent, and twisted. (c) CV curves of $NiCo_2O_4$@PPy NWAs and AC half cells in 3 M KOH solution at a scan rate of 10 mV s^{-1}; (d) CV curves of $NiCo_2O_4$@PPy//AC asymmetric supercapacitor measured at different potential window at a scan rate of 150 mV s^{-1}; (e) CV curves of the asymmetric supercapacitor measured at different scan rates between 0 and 1.6 V; (f) Galvanostatic charge−discharge curves at different current densities between 0 and 1.6 V.

electrolyte infiltration and thus more electro-active sites can be more easily accessible to the electrolyte ions. (iv) The $NiCo_2O_4$ NWAs are served as rigid back-bones to support PPy by interlinking the polymer chains. Thus, the in situ combination of $NiCo_2O_4$ and PPy would give rise to a strong synergetic effect and good mechanical integrity for improving the electrochemical performance. These advantages enable the hybrid $NiCo_2O_4$@PPy electrode to show outstanding properties, such as exceptionally high capacitance, good rate capability, and long cycle life, which are highly desirable for supercapacitor implementation.

To further estimate the $NiCo_2O_4$@PPy NWAs electrode for practical applications, an asymmetric supercapacitor was fabricated using the $NiCo_2O_4$@PPy NWAs and activated carbon (AC) on nickel foam as electrodes (denoted as $NiCo_2O_4$@PPy//AC ASC), as shown in Figure 9a. Excitingly, the as-fabricated supercapacitor shows superior mechanical property of flexibility, which can be folded (top in Figure 9b) and twisted (bottom in Figure 9b) without damaging the structural integrity. For investigating the total voltage of the device, the CV curves collected in a three-electrode system from the AC film electrode and $NiCo_2O_4$@PPy NWAs hybrid electrode in 3 M KOH electrolyte demonstrate that the operating potential windows for AC film and $NiCo_2O_4$@PPy NWAs hybrid electrodes are −1.0−0 V and −0.1−0.6 V (Figure 9c), respectively, which suggest that the ASC device can be operated to 1.6 V. Figure 9d shows the CV curves of the ASC device at different voltage windows varying from 0.6 to 1.6 V. When the voltage is 1.0 V, two weak symmetric broad redox peaks can be observed, which indicate the pseudocapacitive properties of the ASC device is derived from the positive electrode ($NiCo_2O_4$@PPy NWAs). Moreover, when the operating voltage window increases up to 1.6 V, more faradaic reactions occurred. As shown in Figure S9a, the galvanostatic charge−discharge curves of the $NiCo_2O_4$@PPy//AC ASC device with different potential windows at a current density of 8 mA cm^{-2} were also displayed. Significantly, the specific capacitance increases from 12 to 102.5 F g^{-1} when the working voltage window of the device increases from 0.6 to 1.6 V, meanwhile the large potential window range is also beneficial to improve the energy density (Figure S9b). Hence, we have selected an input voltage range of 0−1.6 V to further investigate the performance of the $NiCo_2O_4$@PPy//AC ASC device. To research the influence of scan rate on the electrochemical performance, the rate-dependent CV curves of the $NiCo_2O_4$@PPy//AC ASC device with scan rates from 10 to 500 mV s^{-1} are measured below 1.6 V (Figure 9e). It can be found that the ASC device shows a relatively quasi-rectangular CV shape with weak redox peaks, which indicating that the combination of both EDLC and PC-type presents at all scan rates. Notably, at a high scan rate of 500 mV s^{-1} and a maximum working voltage of 1.6 V, the shape of the CV curve is still well retained, denoting a good rate capability. Figure 9f exhibits the galvanostatic charge−discharge curves within the current density of 1−30 mA cm^{-2} in a voltage window of 0−1.6 V. During the charge−discharge steps, the charge curves of the $NiCo_2O_4$@PPy//AC ASCs are almost symmetric to its corresponding discharge counterpart, even at a high current

DOI: 10.1021/acsami.5b05908
ACS Appl. Mater. Interfaces 2015, 7, 21334−21346

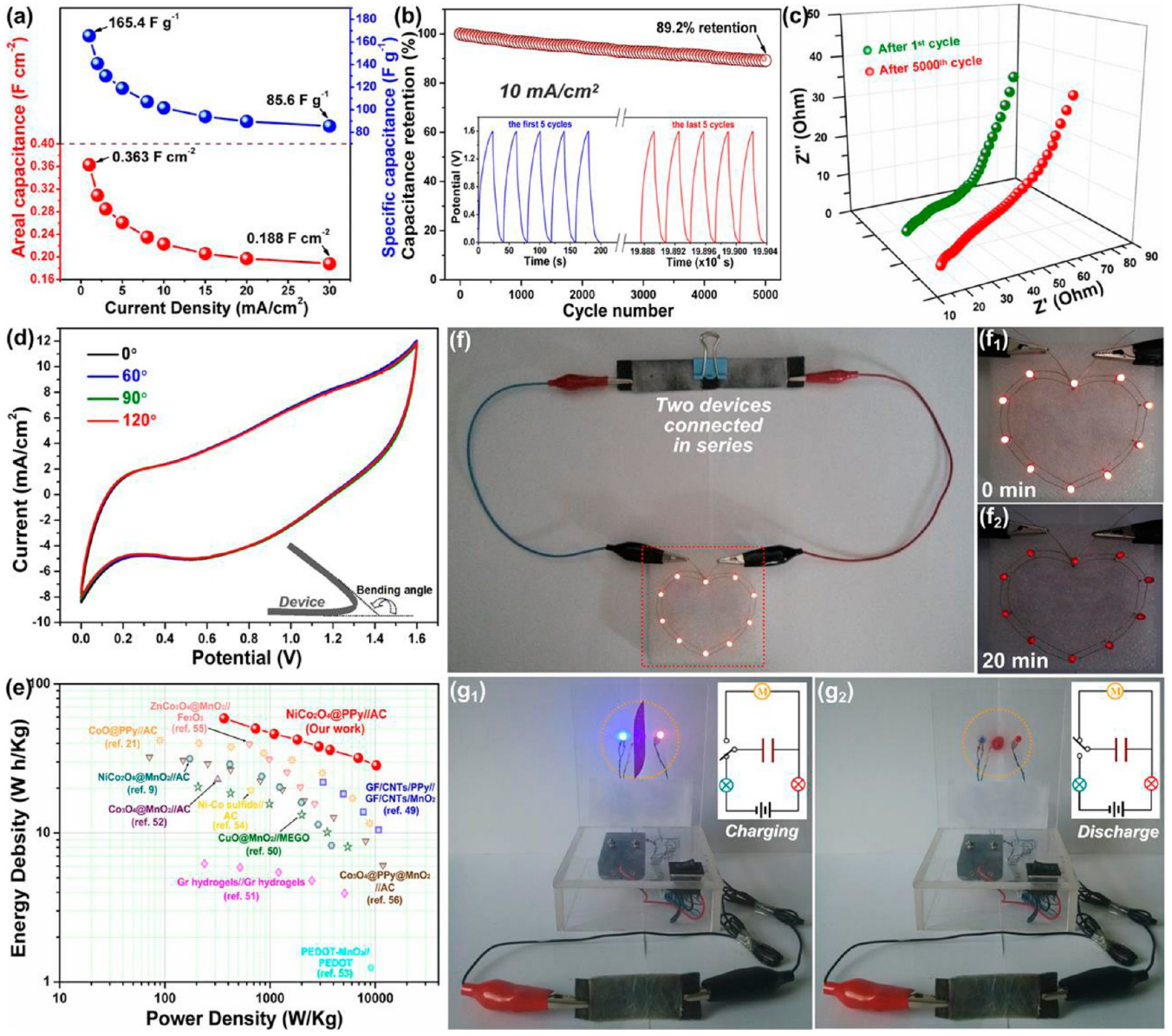

Figure 10. (a) Specific and volumetric capacitance calculated from the charge−discharge curves as a function of current density; (b) cycling performance of ASC devices collected at a scan rate of 10 mA cm^{-2} for 5000 cycles in gel (KOH/PVA) electrolyte, and the inset is charge−discharge curves of the 1st and 5000th cycles for our device; (c) Nyquist plots for the $NiCo_2O_4$@PPy//AC ASC device after the 1st and 5000th cycles; (d) CV curves collected at a scan rate of 200 mV s^{-1} for the ASC device at different bending angles; (e) Ragone plot of the ASCs and some other devices from previous literature for comparison; optical images showing two ASCs connected in series powering (f, f_1, and f_2) LEDs and (g_1 and g_2) a small rotation motor.

density 30 mA cm^{-2}, thus showing the excellent electrochemical performance of the flexile ASCs.

The volumetric capacitance (C_{vc}) at different scan rates are calculated from the discharge curves based on the active area of both electrodes. Figure 10a reveals the current density dependence of the C_{vc} of the hybrid ASC device (red curve); the maximum C_{vc} is ~1.21 F cm^{-3} under a current density of 1 mA/cm^{-2}. Markedly, when the current density rises to 30 mA/cm^{-2}, its C_{vc} continues to remain as high as 0.627 F cm^{-3}. The specific capacitance (C_{sc}) based on the total mass of active materials of two electrodes versus current density plots are also shown in Figure 10a (blue curve). It is noteworthy that the device retains 73% of its initial capacitance (165.4 F g^{-1}) when the scan rate increased from 1 to 30 mA cm^{-2}, which is superior to that of many other AC-based ASCs.[21,48] These results indicate the good rate capability of the $NiCo_2O_4$@PPy//AC ASCs. As depicted in Figure 10b, the cycling lifetime of the $NiCo_2O_4$@PPy//AC ASC device was tested at 10 mA/cm^{-2} in the potential region of 0−1.6 V, which exhibits an excellent long-term stability, and the capacitance loss is only 10.8% after 5000 cycles. Moreover, the charge−discharge curves are almost overlapping between the first and the last 5 cycles (inset of in Figure 10b), which also shows its excellent stability for the ASCs. Figure 10c shows the electrochemical impedance spectroscopy (EIS) of the $NiCo_2O_4$@PPy//AC ASCs in the frequency range of 10^{-2}−10^5 Hz after the 1st and 5000th cycles. The diagonal line in the low frequency part can be assigned to the diffusion-controlled Warburg capacitive behavior, and the semicircle in the high frequency region is attributed to the charge transfer process.[46] The equivalent

DOI: 10.1021/acsami.5b05908
ACS Appl. Mater. Interfaces 2015, 7, 21334−21346

series resistance (ESR) values after the 1st and 5000th cycles are tested to be ~52 and 64 Ω, respectively, and further proves that the exceptional cycling stability of the $NiCo_2O_4$@PPy//AC ASCs.

To demonstrate the potential application of $NiCo_2O_4$@PPy//AC ASC devices in the flexible electronics area, the electrochemical performance of the ASCs at different bending angle conditions is investigated by measuring the corresponding CV curves. As seen in Figure 10d, the CV curves and specific capacitance values of the ASC are nearly the same at various bending angles, indicating the excellent flexibility of the hybrid ASCs. Figure 10e compared the Ragone plot of the $NiCo_2O_4$@PPy//AC ASC and some of previous hybrids devices. Importantly, the $NiCo_2O_4$@PPy//AC ASCs deliver high energy density (58.8 W h kg^{-1} at 365 W kg^{-1}) and excellent power density (10.2 kW kg^{-1} at 28.4 W h kg^{-1}). These values are superior to that of the listed hybrid supercapacitors.[9,21,49−56] To further demonstrate the practical use of the $NiCo_2O_4$@PPy//AC ASC device, two $NiCo_2O_4$@PPy//AC ASCs were connected in series, which can power light-emitting diodes (LEDs) and a fan. The ASCs will provide an output potential window of 3.2 V in series, while ASCs in parallel can offer much longer operating time (see Figure S9c,d). By charging two ASCs in series for only 30 s to ~3.2 V, which can light 10 red LED (1.8 V, 3 mm) indicators efficiently, these red LEDs are able to remain bright enough after 10 min and even effective for display after 20 min (Figure 10f and Figure S9e). More strikingly, it can robustly drive a small motor (3 V, 0.45 W) after charging for a very short time (Figure 10g_1,g_2).

CONCLUSION

In summary, we have designed a highly ordered 3D $NiCo_2O_4$@PPy hybrid NWAs on carbon textiles positive elecrode for SCs application. The high specific capacitance and the superior cycling stability is attributed to the remarkable synergistic contribution from the $NiCo_2O_4$ nanowires and conductive PPy, in which the PPy improves the electron transportation and the mesoporous $NiCo_2O_4$ facilitates the ion diffusion, as a result in enhancing the rate capability. Moreover, a flexible asymmetric supercapacitor device based on 3D $NiCo_2O_4$@PPy hybrid NWAs and activated carbon (AC) is demonstrated, achieving a high energy density of 58.8 W h kg^{-1} at 365 W kg^{-1}. Noteworthy, the capacitance of our device in solid electrolyte achieves ~82.9% retention after 5000 cycles. This work opens up new opportunities for design of a novel composite electrode for next generation high-performance flexible and lightweight supercapacitors

ASSOCIATED CONTENT

Supporting Information

The Supporting Information is available free of charge on the ACS Publications website at DOI: 10.1021/acsami.5b05908.

Additional optical images for the flexible electrode materials; molecular formula, SEM images, and TEM images of pure PPy; XPS spectra of $NiCo_2O_4$@PPy NWAs; SEM images and scheme of the $NiCo_2O_4$ NWAs at various reaction stages; SEM images of the $NiCo_2O_4$@PPy NFAs synthesized at different times; galvanostatic charge−discharge curves for different electrode materials; detailed CV curves and charge−discharge profiles of the $NiCo_2O_4$ NWAs and Coulombic efficiency and EIS of $NiCo_2O_4$@PPy NWAs; galvanostatic charge−discharge profiles collected at different potential windows for the $NiCo_2O_4$@PPy//AC ASC device, specific capacitance, and energy density calculated for the $NiCo_2O_4$@PPy//AC ASC device; galvanostatic charge−discharge curves of the single ASC and two ASCs connected in series or in parallel, and pictures of the 10 red LEDs at different stages (PDF)

AUTHOR INFORMATION

Corresponding Authors

*(C.C.) Tel./fax: +86-21-65988636. E-mail: cwcheng@tongji.edu.cn.

*(H.Y.Y.) Tel.: +65- 63036600. E-mail: yanghuiying@sutd.edu.sg.

Notes

The authors declare no competing financial interest.

ACKNOWLEDGMENTS

This work is finacially supported by 973 Program (2013CB632701) and NSFC grant (51202163). H.Y.Y. acknowledges the SUTD-MIT international design center support (IDG21400109).

REFERENCES

(1) Cao, Q.; Kim, H. S.; Pimparkar, N.; Kulkarni, J. P.; Wang, C.; Shim, M.; Roy, K.; Alam, M. A.; Roger, J. A. Medium-Scale Carbon Nanotube Thin-Film Integrated Circuits on Flexible Plastic Substrates. *Nature* **2008**, *454*, 495−500.

(2) Ju, S.; Facchetti, A.; Xuan, Y.; Liu, J.; Ishikawa, F.; Ye, P.; Zhou, C.; Marks, T. J.; Janes, D. B. Fabrication of Fully Transparent Nanowire Transistors for Transparent and Flexible Electronics. *Nat. Nanotechnol.* **2007**, *2*, 378−384.

(3) Kim, D.-H.; Lu, N.; Ma, R.; Kim, Y.-S.; Kim, R.-H.; Wang, S.; Wu, J.; Won, S. M.; Tao, H.; Islam, A.; et al. Epidermal Electronics. *Science* **2011**, *333*, 838−843.

(4) Xu, Y. X.; Lin, Z. Y.; Huang, X. Q.; Liu, Y.; Huang, Y.; Duan, X. F. Flexible Solid-State Supercapacitors Based on Three-Dimensional Graphene Hydrogel Films. *ACS Nano* **2013**, *7*, 4042−4049.

(5) Miller, J. R.; Simon, P. Electrochemical Capacitors for Energy Management. *Science* **2008**, *321*, 651−652.

(6) Wang, G. P.; Zhang, L.; Zhang, J. J. A Review of Electrode Materials for Electrochemical Supercapacitors. *Chem. Soc. Rev.* **2012**, *41*, 797−828.

(7) Liu, J. P.; Jiang, J.; Cheng, C. W.; Li, H. X.; Zhang, J. X.; Gong, H.; Fan, H. J. Co_3O_4 Nanowire@MnO_2 Ultrathin Nanosheet Core/Shell Arrays: A New Class of High-Performance Pseudocapacitive Materials. *Adv. Mater.* **2011**, *23*, 2076−2081.

(8) Kong, D. Z.; Luo, J. S.; Wang, Y. L.; Ren, W. N.; Yu, T.; Luo, Y. S.; Yang, Y. P.; Cheng, C. W. Three-Dimensional Co_3O_4@MnO_2 Hierarchical Nanoneedle Arrays: Morphology Control and Electrochemical Energy Storage. *Adv. Funct. Mater.* **2014**, *24*, 3815−3826.

(9) Xu, K. B.; Li, W. Y.; Liu, Q.; Li, B.; Liu, X. J.; An, L.; Chen, Z. G.; Zou, R. J.; Hu, J. Q. Hierarchical Mesoporous $NiCo_2O_4$@MnO_2 Core-Shell Nanowire Arrays on Nickel Foam for Aqueous Asymmetric Supercapacitors. *J. Mater. Chem. A* **2014**, *2*, 4795−4802.

(10) Wang, Y.; Yu, S. F.; Sun, C. Y.; Zhu, T. J.; Yang, H. Y. MnO_2/Onion-Like Carbon Nanocomposites for Pseudocapacitors. *J. Mater. Chem.* **2012**, *22*, 17584−17588.

(11) Lu, X. H.; Yu, M. H.; Wang, G. M.; Zhai, T.; Xie, S. L.; Ling, Y. C.; Tong, Y. X.; Li, Y. H-TiO_2@MnO_2//H-TiO_2@C Core-Shell Nanowires for Figh Performance and Flexible Asymmetric Supercapacitors. *Adv. Mater.* **2013**, *25*, 267−272.

(12) Fan, Z. J.; Yan, J.; Wei, T.; Zhi, L. J.; Ning, G. Q.; Li, T. Y.; Wei, F. Asymmetric Supercapacitors Based on Graphene/MnO_2 and

DOI: 10.1021/acsami.5b05908
ACS Appl. Mater. Interfaces 2015, 7, 21334−21346

Activated Carbon Nanofiber Electrodes with High Power and Energy Density. *Adv. Funct. Mater.* **2011**, *21*, 2366−2375.
(13) Wu, Z. S.; Ren, W. C.; Wang, D. W.; Li, F.; Liu, B. L.; Cheng, H. M. High-Energy MnO_2 Nanowire/Graphene and Graphene Asymmetric Electrochemical Capacitors. *ACS Nano* **2010**, *4*, 5835−5842.
(14) Wang, Q. F.; Wang, X. F.; Liu, B.; Yu, G.; Hou, X. J.; Chen, D.; Shen, G. Z. $NiCo_2O_4$ Nanowire Arrays Supported on Ni Foam for High-Performance Flexible All-Solid-State Supercapacitors. *J. Mater. Chem. A* **2013**, *1*, 2468−2473.
(15) Zhang, G. Q.; Wu, H. B.; Hoster, H. E.; Chan-Park, M. B.; Lou, X. W. Single-Crystalline NiCo2O4 Nanoneedle Arrays Grown on Conductive Substrates as Binder-Free Electrodes for High-Performance Supercapacitors. *Energy Environ. Sci.* **2012**, *5*, 9453−9456.
(16) Wang, H. L.; Gao, Q. M.; Jiang, L. Facile Approach to Prepare Nickel Cobaltite Nanowire Materials for Supercapacitors. *Small* **2011**, *7*, 2454−2459.
(17) Zhou, W. W.; Kong, D. Z.; Jia, X. T.; Ding, C. Y.; Cheng, C. W.; Wen, G. W. $NiCo_2O_4$ Nanosheet Supported Hierarchical Core-Shell Arrays for High-Performance Supercapacitors. *J. Mater. Chem. A* **2014**, *2*, 6310−6315.
(18) Shang, C. Q.; Dong, S. M.; Wang, S.; Xiao, D. D.; Han, P. X.; Wang, X. G.; Gu, L.; Cui, G. L. Coaxial $Ni_xCo_{2x}(OH)_{6x}$/TiN Nanotube Arrays as Supercapacitor Electrodes. *ACS Nano* **2013**, *7*, 5430−5436.
(19) Huang, L.; Chen, D. C.; Ding, Y.; Feng, S.; Wang, Z. L.; Liu, M. L. Nickel-Cobalt Hydroxide Nanosheets Coated on $NiCo_2O_4$ Nanowires Grown on Carbon Fiber Paper for High-Performance Pseudocapacitors. *Nano Lett.* **2013**, *13*, 3135−3139.
(20) Chen, H.; Hu, L. F.; Chen, M.; Yan, Y.; Wu, L. M. Nickel-Cobalt Layered Double Hydroxide Nanosheets for High-Performance Supercapacitor Electrode Materials. *Adv. Funct. Mater.* **2014**, *24*, 934−942.
(21) Zhou, C.; Zhang, Y. W.; Li, Y. Y.; Liu, J. P. Construction of High-Capacitance 3D CoO@Polypyrrole Nanowire Array Electrode for Aqueous Asymmetric Supercapacitor. *Nano Lett.* **2013**, *13*, 2078−2085.
(22) Yu, M. H.; Zeng, Y. X.; Zhang, C.; Lu, Z. H.; Zeng, C. H.; Yao, C. Z.; Yang, Y. Y.; Tong, Y. X. Titanium Dioxide@Polypyrrole Core-Shell Nanowires for All Solid-State Flexible Supercapacitors. *Nanoscale* **2013**, *5*, 10806−10810.
(23) Snook, G. A.; Kao, P.; Best, A. S. Conducting-Polymer-Based Supercapacitor Devices and Electrodes. *J. Power Sources* **2011**, *196*, 1−12.
(24) Zhang, X.; Yang, W. S.; Ma, Y. W. Synthesis of Polypyrrole-Intercalated Layered Manganese Cxide Manocomposite by A Delamination/Reassembling Method and Its Electrochemical Capacitance Performance. *Electrochem. Solid-State Lett.* **2009**, *12*, A95−A98.
(25) Tang, Z.; Tang, C. H.; Gong, H. A. High Energy Density Asymmetric Supercapacitor from Nano-Architectured $Ni(OH)_2$/Carbon Nanotube Electrodes. *Adv. Funct. Mater.* **2012**, *22*, 1272−1278.
(26) Singh, A. K.; Sarkar, D.; Khan, G. G.; Mandal, K. Unique Hydrogenated Ni/NiO Core/Shell 1D Nano-Heterostructures with Superior Electrochemical Performance as Supercapacitors. *J. Mater. Chem. A* **2013**, *1*, 12759−12767.
(27) Liu, J. L.; Zhang, L. L.; Wu, H. B.; Lin, J. Y.; Shen, Z. X.; Lou, X. W. High-Performance Flexible Asymmetric Supercapacitors Based on A New Graphene Foam/Carbon Nanotube Hybrid Film. *Energy Environ. Sci.* **2014**, *7*, 3709−3719.
(28) Yan, J.; Fan, Z. J.; Sun, W.; Ning, G. Q.; Wei, T.; Zhang, Q.; Zhang, R. F.; Zhi, L. J.; Wei, F. Advanced Asymmetric Supercapacitors Based on $Ni(OH)_2$/Graphene and Porous Graphene Electrodes with High Energy Density. *Adv. Funct. Mater.* **2012**, *22*, 2632−2641.
(29) Wang, H. W.; Wang, X. F. Growing Nickel Cobaltite Nanowires and Nanosheets on Carbon Cloth with Different Pseudocapacitive Performance. *ACS Appl. Mater. Interfaces* **2013**, *5*, 6255−6260.
(30) Mao, L.; Chan, H. S. O.; Wu, J. S. Cetyltrimethylammonium Bromide Intercalated Graphene/Polypyrrole Nanowire Composites for High Performance Supercapacitor Electrode. *RSC Adv.* **2012**, *2*, 10610−10617.
(31) Liu, W. W.; Lu, C. X.; Liang, K.; Tay, B. K. A Three Dimensional Vertically Aligned Multiwall Carbon Nanotube/$NiCo_2O_4$ Core/Shell Structure for Novel High-Performance Supercapacitors. *J. Mater. Chem. A* **2014**, *2*, 5100−5107.
(32) Du, J.; Zhou, G.; Zhang, H. M.; Cheng, C.; Ma, J. M.; Wei, W. F.; Chen, L. B.; Wang, T. H. Ultrathin Porous $NiCo_2O_4$ Nanosheet Arrays on Flexible Carbon Fabric for High-Performance Supercapacitors. *ACS Appl. Mater. Interfaces* **2013**, *5*, 7405−7409.
(33) Yang, G. W.; Xu, C. L.; Li, H. L. Electrodeposited Nickel Hydroxide on Nickel Foam with Ultrahigh Capacitance. *Chem. Commun.* **2008**, *48*, 6537−6539.
(34) Huang, L.; Chen, D. C.; Ding, Y.; Wang, Z. L.; Zeng, Z. Z.; Liu, M. L. Hybrid Composite $Ni(OH)_2$@$NiCo_2O_4$ Grown on Carbon Fiber Paper for High-Performance Supercapacitors. *ACS Appl. Mater. Interfaces* **2013**, *5*, 11159−11162.
(35) Janáky, C.; de Tacconi, N. R.; Chanmanee, W.; Rajeshwar, K. Bringing Conjugated Polymers and Cxide Nanoarchitectures into Intimate Contact: Light-Induced Electrodeposition of Polypyrrole and Polyaniline on Nanoporous WO_3 or TiO_2 Nanotube Array. *J. Phys. Chem. C* **2012**, *116*, 19145−19155.
(36) Liu, J. L.; Zhou, W. W.; Lai, L. F.; Yang, H. P.; Lim, S. H.; Zhen, Y. D.; Yu, T.; Shen, Z. X.; Lin, J. Y. Three Dimensionals α-Fe_2O_3@ Polypyrrole (Ppy) Nanoarray as Anode for Micro Lithium Ion Batteries. *Nano Energy* **2013**, *2*, 726−732.
(37) Yuan, C.; Li, J.; Hou, L.; Zhang, X.; Shen, L.; Lou, X. W. Ultrathin Mesoporous $NiCo_2O_4$ Nanosheets Supported on Ni Foam As Advanced Electrodes for Supercapacitors. *Adv. Funct. Mater.* **2012**, *22*, 4592−4597.
(38) Lei, Y.; Li, J.; Wang, Y. Y.; Gu, L.; Chang, Y. F.; Yuan, H. Y.; Xiao, D. Rapid Microwave-Assisted Green Synthesis of 3D Hierarchical Flower-Shaped $NiCo_2O_4$ Microsphere for High-Performance Supercapacitor. *ACS Appl. Mater. Interfaces* **2014**, *6*, 1773−1780.
(39) Zinovyeva, V. A.; Vorotyntsev, M. A.; Bezverkhyy, I.; Chaumont, D.; Hierso, J. C. Highly Dispersed Palladium-Polypyrrole Nanocomposites: In-Water Synthesis and Application for Catalytic Arylation of Heteroaromatics by Direct C-H Bond Activation. *Adv. Funct. Mater.* **2011**, *21*, 1064−1075.
(40) Chen, L. F.; Zhang, X. D.; Liang, H. W.; Kong, M. G.; Guan, Q. F.; Chen, P.; Wu, Z. Y.; Yu, S. H. Synthesis of Nitrogen-Doped Porous Carbonn Anofibers as An Efficient Electrode Material for Supercapacitors. *ACS Nano* **2012**, *6*, 7092−7102.
(41) Yu, P. P.; Zhao, X.; Huang, Z. L.; Li, Y. Z.; Zhang, Q. H. Free-Standing Three-Dimensional Graphene and Polyaniline Nanowire Arrays Hybrid Foams for High-Performance Flexible and Lightweight Supercapacitors. *J. Mater. Chem. A* **2014**, *2*, 14413−14420.
(42) Shao, J.; Li, X. Y.; Zhang, L.; Qu, Q. T.; Zheng, H. H. Core-Shell Sulfur@Polypyrrole Composites as High-Capacity Materials for Aqueous Rechargeable Batteries. *Nanoscale* **2013**, *5*, 1460−1464.
(43) Xiao, J. W.; Wan, L.; Yang, S. H.; Xiao, F.; Wang, S. Design Hierarchical Electrodes with Highly Conductive $NiCo_2S_4$ Nanotube Arrays Grown on Carbon Fiber Paper for High-Performance Pseudocapacitors. *Nano Lett.* **2014**, *14*, 831−838.
(44) Shen, L. F.; Che, Q.; Li, H. S.; Zhang, X. G. Mesoporous $NiCo_2O_4$ Nanowire Arrays Grown on Carbon Textiles as Binder-Free Flexible Electrodes for Energy Storage. *Adv. Funct. Mater.* **2014**, *24*, 2630−2637.
(45) Wang, J. G.; Yang, Y.; Huang, Z. H.; Kang, F. Y. MnO_2/Polypyrrole Nanotubular Composites: Reactive Template Synthesis, Characterization and Application as Superior Electrode Materials for High-Performance Supercapacitors. *Electrochim. Acta* **2014**, *130*, 642−649.
(46) Kong, D. Z.; Ren, W. N.; Luo, Y. S.; Yang, Y. P.; Cheng, C. W. Scalable Synthesis of Graphene-Wrapped $Li_4Ti_5O_{12}$ Dandelion-Like Microspheres for Lithium-Ion Batteries with Excellent Rate Capability and Long-Cycle Life. *J. Mater. Chem. A* **2014**, *2*, 20221−20230.
(47) Kuang, M.; Zhang, Y. X.; Li, T. T.; Li, K. F.; Zhang, S. M.; Li, G.; Zhang, W. Tunable Synthesis of Hierarchical $NiCo_2O_4$ Nano-

DOI: 10.1021/acsami.5b05908
ACS Appl. Mater. Interfaces 2015, 7, 21334−21346

sheets-Decorated Cu/CuO_x Nanowires Architectures for Asymmetric Electrochemical Capacitors. *J. Power Sources* **2015**, *283*, 270−278.
(48) Zhai, T.; Wang, F.; Yu, M.; Xie, S.; Liang, C.; Li, C.; Xiao, F.; Tang, R.; Wu, Q.; Lu, X.; Tong, Y. 3D MnO_2-Graphene Composites with Large Areal Capacitance for High-Performance Asymmetric Supercapacitors. *Nanoscale* **2013**, *5*, 6790−6796.
(49) Zhu, J. H.; Jiang, J.; Sun, Z. P.; Luo, J. S.; Fan, Z. X.; Huang, X. T.; Zhang, H.; Yu, T. 3D Carbon/Cobalt-Nickel Mixed-Oxide Hybrid Nanostructured Arrays for Asymmetric Supercapacitors. *Small* **2014**, *10*, 2937−2945.
(50) Huang, M.; Zhang, Y.; Li, F.; Wang, Z.; Alamusi; Wen, Z.; Liu, Q.; Hu, N. Merging of Kirkendall Growth and Ostwald Ripening: CuO@MnO_2 Core-Shell Architectures for Asymmetric Supercapacitors. *Sci. Rep.* **2014**, *4*, 4518.
(51) Xu, Y. X.; Lin, Z. Y.; Huang, X. Q.; Liu, Y.; Huang, Y.; Duan, X. F. Flexible Solid-State Supercapacitors Based on Three-Dimensional Graphene Hydrogel Films. *ACS Nano* **2013**, *7*, 4042−4049.
(52) Huang, M.; Zhang, Y. X.; Li, F.; Zhang, L. L.; Wen, Z. Y.; Liu, Q. Facile Synthesis of Hierarchical Co_3O_4@MnO_2 Core-Shell Arrays on Ni Foam for Asymmetric Supercapacitors. *J. Power Sources* **2014**, *252*, 98−106.
(53) Duay, J.; Gillette, E.; Liu, R.; Lee, S. B. Highly Flexible Pseudocapacitor Based on Freestanding Heterogeneous MnO_2/Conductive Polymer Nanowire Arrays. *Phys. Chem. Chem. Phys.* **2012**, *14*, 3329−3337.
(54) Li, Y. H.; Cao, L. J.; Qiao, L.; Zhou, M.; Yang, Y.; Xiao, P.; Zhang, Y. H. Ni-Co Sulfide Nanowires on Nickel Foam with Ultrahigh Capacitance for Asymmetric Supercapacitors. *J. Mater. Chem. A* **2014**, *2*, 6540−6548.
(55) Ma, W. Q.; Nan, H. H.; Gu, Z. X.; Geng, B. Y.; Zhang, X. J. Superior Performance Asymmetric Supercapacitors Based on $ZnCo_2O_4$@MnO_2 Core-Shell Electrode. *J. Mater. Chem. A* **2015**, *3*, 5442−5448.
(56) Han, L. J.; Tang, P. Y.; Zhang, L. Hierarchical Co_3O_4@PPy@MnO_2 Core-Shell-Shell Nanowire Arrays for Enhanced Electrochemical Energy Storage. *Nano Energy* **2014**, *7*, 42−51.

DOI: 10.1021/acsami.5b05908
ACS Appl. Mater. Interfaces 2015, 7, 21334−21346